Journal of Crystal Growth 576 (2021) 126384

Contents lists available at ScienceDirect

Journal of Crystal Growth

journal homepage: www.elsevier.com/locate/jcrysgro

Physically-based, lumped-parameter models for the prediction of oxygen concentration during Czochralski growth of silicon crystals

Kerry Wang [a], Holger Koch [b], Matthias Trempa [b], Christian Kranert [b], Jochen Friedrich [b], Jeffrey J. Derby [a,*]

[a] Department of Chemical Engineering and Materials Science, University of Minnesota, Minneapolis, MN 55455, USA
[b] Fraunhofer IISB, Schottkystraße 10, 91058 Erlangen, Germany

ARTICLE INFO

Communicated by Chung wen Lan

Keywords:
A1. Convection
A1. Computer simulation
A2. Czochralski method
A2. Single Crystal Growth
B2. Semiconducting silicon

ABSTRACT

Lumped-parameter models are derived from boundary layer and other physical arguments to describe oxygen concentration levels during the Czochralski (CZ) growth of silicon. These models are assessed against predictions from a detailed, high-fidelity 2D-3D numerical simulation of the entire CZ puller, whose solutions are realistic but require intense computational effort. Comparisons of predictions show that the lumped-parameter model captures the correct trends of melt oxygen levels influenced by melt height, crucible rotation, and crystal rotation. A simple fitting of coefficients provides reasonably good quantitative predictions by the lumped-parameter model, and its near-instantaneous computations make it an interesting candidate for real-time growth optimization and control. Possible model improvements and extensions are discussed.

1. Introduction

Crystal growth models have been applied to better understand the Czochralski (CZ) growth of silicon, ranging from early two-dimensional (2D), thermal-capillary models [1–9] to modern models that employ three-dimensional (3D) large-eddy simulation (LES) to represent turbulence in large-scale CZ melts [10–18]. Modeling has been particularly useful to complement challenging, expensive growth experiments in large-diameter CZ silicon systems. Recent approaches have employed a combination of global, quasi-stationary, 2D axisymmetric models for heat transfer within the CZ puller with local, three-dimensional (3D), time-dependent models for the melt-crystal-crucible regions [14,15].

However, high-fidelity, computational models for CZ silicon growth are also complex and expensive, often taking several weeks on high-performance computing clusters to calculate quantities of interest, such as oxygen distributions in the growing crystal [14,15]. Simpler models, requiring less computational effort, would be desirable for a rapid estimation of the influence of process parameters on the crystal properties, such as for process optimization or model-based control [19–22].

A much simpler approach to model engineering systems involving transport is the *lumped-parameter model,* where a complex problem involving spatially varying quantities, normally described by partial differential equations, is described by applying simplifying assumptions about fluxes and mixing to arrive at a system of time-dependent ordinary differential equations or steady-state algebraic equations that require far less solution effort. Historically, such lumped-parameter models have yielded great insight when computational power could not yet feasibly be applied for solution of the spatially distributed system, such as in the analysis of the dynamics of stirred-tank chemical reactors [23–26]. Such models have also been applied to model the Czochralski crystal growth process. Gevelber et al. [19,20] derived a lumped element representation of heat transfer in a CZ process to predict system response to disturbances and inputs. Carlberg et al. [27] and Hoshikawa and Huang [28] employed boundary layer and mixing models to describe oxygen transport in Czochralski growth of silicon. Recently, Friedrich et al. [29] developed a lumped-parameter model to describe oxygen transport in a large-scale CZ silicon growth system.

In this work, we aim to advance the model of Friedrich et al. [29] so that it better represents the effects of crystal rotation and is capable of more accurate predictions. We present a discussion of model development followed by an assessment of the ability of the lumped-parameter model to correlate data provided by extensive 2D-3D simulations of a large-scale CZ puller.

* Corresponding author.
E-mail address: derby@umn.edu (J.J. Derby).

https://doi.org/10.1016/j.jcrysgro.2021.126384
Received 25 August 2021; Received in revised form 5 October 2021; Accepted 11 October 2021
Available online 19 October 2021

2. Modeling approaches

2.1. High-fidelity model

We performed coupled, 2D-3D simulations of heat and oxygen transport during the Czochralski growth of silicon single crystals of 210 mm diameter and 100 kg weight in a 24-inch-diameter silica crucible. In the 2D-3D model, the convective heat and oxygen transfer are computed by a time-dependent, 3D-LES model [13,14]. Thermal boundary conditions for the 3D model are provided by computing the 2D global heat transfer in the furnace, initially calculated without the effects of convection in the melt. Once available from the 3D calculations, temperatures and velocities are averaged azimuthally at each time step. The resulting distribution of convective velocity, turbulent heat fluxes, and effective thermal conductivity are then provided to a Reynolds-averaged form of the heat transfer equation inside the 2D model, and the results are iterated until boundary conditions match. Oxygen transport is also calculated by the coupled 2D-3D approach using an analogous approach. Azimuthally-averaged concentration distributions from the 3D model provide turbulent transport coefficients to the 2D Reynolds-averaged species transport model. A flux balance involving SiO is imposed at the free melt surface, and iterations are performed until this flux matches between both models. The details of the model can be found in [13,30,14], and material properties of silicon used in the simulations can be found in [14].

The combined model is implemented into the programs CrysMAS [31] for the global 2D model and OpenFOAM [32] for the local 3D model. This 2D-3D model has been validated by comparison to data from direct numerical simulation (DNS) model predictions, as well as by comparison to experimental data. The high-fidelity 2D-3D model was shown to accurately predict the shape of the melt-crystal interface and the oxygen distribution in large-diameter Si CZ crystals [13,14], as well as the limitations of the growth rate during pulling of large diameter CZ Si crystals with respect to the twisting phenomena [15].

2.2. Lumped-parameter model

We extend the previous analyses of Carlberg et al. [27], Hoshikawa and Huang [28], and Friedrich et al. [29] to arrive at new lumped-parameter models for oxygen transport during large-scale Czochralski silicon growth. Fig. 1 schematically represents the models that we employ in this study, and Table 1 lists the primary mathematical variables of the lumped-parameter model.

We assume that the melt is well mixed throughout the bulk due to

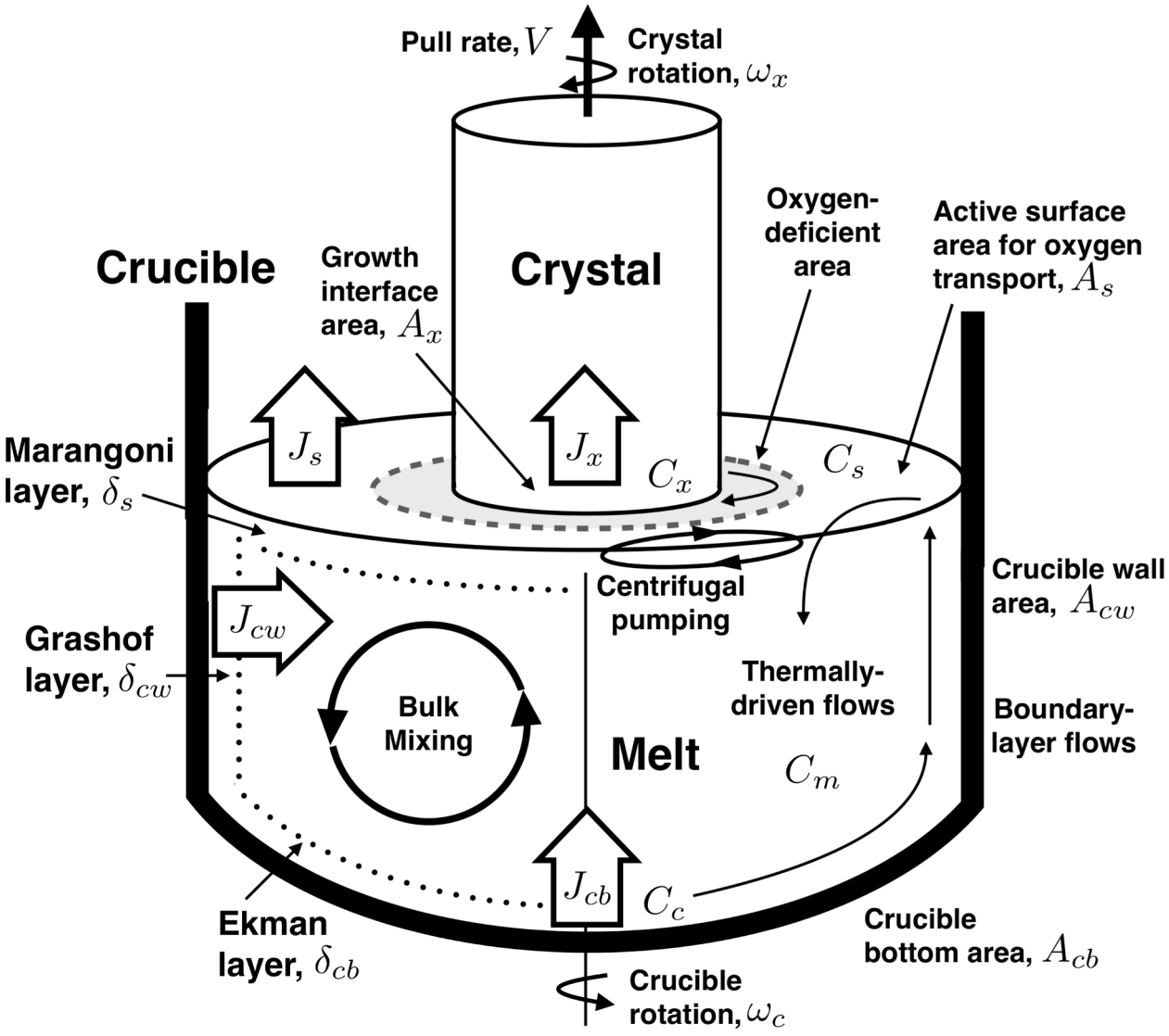

Fig. 1. A schematic depiction of oxygen transport in a Czochalski silicon growth system in our lumped-parameter models. Indicated model variables are described in Table 1.

Table 1
Descriptions of variables appearing in Fig. 1 for our lumped-parameter models of oxygen transport during CZ silicon crystal growth. Subscripts $i = c, cw, cb, s, m$, and x refer to crucible, crucible wall, crucible bottom, melt free-surface, melt bulk, and crystal, respectively. Additional mathematical variables are defined as they occur in the text.

Quantity	Description
C_c	Equilibrium oxygen concentration at crucible wall
C_m	Oxygen concentration in the melt bulk
C_s	Oxygen concentration along the melt free-surface
C_x	Oxygen concentration in the crystal at the melt-crystal interface
A_{cw}	Contact area between melt and crucible wall
A_{cb}	Contact area between melt and crucible bottom
A_s	Active area for oxygen transport across the melt free-surface
A_x	Area of melt-crystal interface
r_c	Crucible radius
r_x	Crystal radius
δ_i'	Momentum boundary layer thickness
J_i	Molar oxygen flux
V	Crystal pull rate
ω_i	Angular velocity of rotation

turbulent, buoyancy-driven flows. The concentration of oxygen in the well-mixed melt region is calculated by the balance of oxygen flows into and out of the bulk of melt. These flows are determined by computing oxygen fluxes and surface areas over which these fluxes occur. Furthermore, the fluxes are computed by assuming diffusion across solute boundary layers, whose thicknesses scale with corresponding strengths of buoyant flows, flows driven by rotation of crystal and crucible, and Marangoni flows that arise from surface-tension gradients. These boundary layers are presumed to be laminar in character and embedded within turbulent layers.

The exact nature of the dissolved, oxygen in liquid silicon, whether SiO, atomic oxygen, or other oxygen-containing species, is still unclear [33]; however, we simply consider the melt to be a well-mixed reservoir and perform an oxygen atom balance to give,

$$\frac{d(V_m C_m)}{dt} = J_{cw}A_{cw} + J_{cb}A_{cb} - J_s A_s - J_x A_x, \tag{1}$$

where V_m is the melt volume, C_m is the oxygen concentration in the well-mixed melt, and J_i and A_i are oxygen fluxes and areas corresponding to surfaces i, with cw and cb referring to the crucible side wall and bottom, respectively, s referring to the melt free-surface, and x denoting the melt-crystal interface. A negative sign preceding a term indicates oxygen flowing out of the melt, and a positive sign indicates oxygen flowing into the melt. The calculation of the different fluxes, J_i, and areas, A_i, in this equation are described in the following sections.

In general, we argue that oxygen fluxes across the various surfaces that bound the well-mixed melt can be approximated by diffusive transport through solute boundary layers and represented as follows,

$$J_i = \frac{D}{\delta_i}(C_m - C_i), \tag{2}$$

where D is a diffusion coefficient for oxygen in liquid silicon, δ_i is the solute boundary layer width, and C_i is the concentration of oxygen along surface i.

Solute boundary layer thicknesses are estimated from hydrodynamic, or momentum, boundary layers, according to the scaling derived from classical boundary layer analysis,

$$\delta_i \sim 2.4 Sc^{-1/3}\delta_i', \tag{3}$$

where the Schmidt number is defined as $Sc = \nu/D$, with ν representing the kinematic viscosity of the liquid and D the diffusion coefficient for oxygen in liquid silicon. The variable δ_i' represents the hydrodynamic boundary layer for the surface i, which will be derived via scaling from fluid dynamics, as discussed in the following sections. The scaling dependence of the solute boundary layer on the Schmidt number was originally derived via boundary layer theory [34,35], and the prefactor value of 2.4 is taken from the analysis of Vartak et al. [36].

2.2.1. Crucible fluxes and areas

We argue that rapid dissolution of the quartz glass crucible liner by the high-temperature molten silicon sets the local oxygen concentration at an equilibrium value [12,37–40] along the inner crucible wall. The temperature-dependent values from Smirnov et al. [12] are applied as the boundary condition for C_c in the coupled 2D-3D computations [14]. However, changes in the oxygen equilibrium concentration for the different wall temperatures considered here are less than 3% [40], so we simply apply a constant value of C_c for our lumped-parameter model; this value is listed with all other model variables in Table 2.

To estimate the solute boundary layer thicknesses, δ_i, we first consider the thickness of hydrodynamic or momentum boundary layers for the velocity field. As a proxy for buoyant and rotational flows in the CZ crucible, we turn to the analysis by King et al. [41], who investigated different flow regimes in rotating Rayleigh–Benard configurations. This problem is described by two dimensionless groups, the Ekman number, Ek, and Rayleigh number, Ra, which are defined for the present work as follows:

$$Ek = \frac{\nu}{2\omega_c r_c^2}, \tag{4}$$

where ν is the kinematic viscosity of the liquid, ω_c is the angular rotation of the crucible, and r_c is the crucible inner radius, and

$$Ra = \frac{\beta g \Delta T r_c^3}{\alpha\nu} = GrPr, \tag{5}$$

with β representing the volumetric expansion coefficient of liquid silicon, g as the gravitational acceleration constant, ΔT as the maximum

Table 2
Values used in the lumped-parameter models for oxygen transport during CZ silicon crystal growth.

	Value	Comments
D	5×10^{-8} m^2/s	Diffusivity of oxygen species in liquid silicon
ρ_s	2329 kg/m^3	Density of solid silicon
ρ_m	2520 kg/m^3	Density of liquid silicon
ν	3×10^{-7} m^2/s	Kinematic viscosity of liquid silicon
α	2.90×10^{-5} m^2/s	Thermal diffusivity of liquid silicon
β	1.44×10^{-4} K^{-1}	Thermal expansivity of liquid silicon
$\frac{\partial\sigma}{\partial T}$	2.80×10^{-4} N/mK	Temperature-derivative of surface tension of liquid silicon
k	1.2	Equilibrium distribution coefficient for oxygen in silicon
g	9.81m/s^2	Gravitational acceleration
T_m	1683 K	Melting temperature of silicon
ΔT	26.0–60.2 K	Temperature difference across melt, from 2D-3D model
r_c	0.6096 m	Crucible radius
r_x	0.1050 m	Crystal radius
ω_c	5–15 rpm	Angular rotation rate of crucible (counter-clockwise)
ω_x	4–30 rpm	Angular rotation rate of crystal (clockwise)
B_{Ek}	4.65	Coefficient for Ekman layer, dimensionless
B_{Gr}	0.072	Coefficient for Grashof layer, dimensionless
B_{Ma}	1.0	Coefficient for Marangoni layer, dimensionless
B_A	0.067	Coefficient for active surface area, dimensionless
C_c	2×10^{18} atoms/cm^{-3}	Oxygen concentration along the inner crucible surface
C_s	0 atoms/cm^{-3}	Oxygen concentration along the melt free-surface
V	1.67×10^{-5} m/s	Crystal pull rate

temperature difference over the melt, and α as the thermal diffusivity of the liquid. As indicated in the above definition, the Rayleigh number can also be expressed as the product of the Grashof number, Gr, and Prandtl number, $Pr = \alpha/\nu$.

King et al. [41] showed that geostrophic flows, namely those that satisfy the criterion $RaEk^{3/2} < 10$, exhibit a momentum boundary layer thickness that scales as,

$$\delta_{Ek}^{'} \sim 3Ek^{1/2}L, \tag{6}$$

where L is the characteristic length scale for the system, taken here as the radius of the crucible r_c. For the Czochralski system considered in this study, $RaEk^{3/2} \sim 10^{-8}$, clearly satisfying the geostrophic condition.

We consider two different representations of solute boundary layers along the crucible for our lumped-parameter model. The first approach, which we simply denote as the Ek lumped-parameter model, presumes that the Ekman layer scaling describes the hydrodynamic boundary layers along all crucible surfaces, so that the solute boundary thickness is given as,

$$\delta_{cw} = \delta_{cb} = 2.4B_{Ek}Sc^{-1/3}Ek^{1/2}r_c, \tag{7}$$

where B_{Ek} is a constant whose value should be approximately three, from Eq. (6) above, and with r_c, the crucible inner radius, chosen as the characteristic length scale.

We argue that the flows in a Czochralski melt likely produce boundary layers of different thicknesses along vertical and horizontal crucible walls and put forth a second approach, which we denote as the $Ek + Gr$ lumped-parameter model. Here, we separately estimate the viscous boundary layer along the vertical crucible wall from analyses of buoyant convection in an enclosed domain [42,7] as,

$$\delta_{Gr}^{'} \sim Pr^{-1/4}Gr^{-1/4}L, \tag{8}$$

where we again set the characteristic distance $L = r_c$.

In the $Ek + Gr$ model, we then compute different solute boundary layer thicknesses for the crucible wall and crucible bottom as,

$$\delta_{cw} = 2.4B_{Gr}Sc^{-1/3}Gr^{-1/4}r_c, \tag{9}$$

$$\delta_{cb} = 2.4B_{Ek}Sc^{-1/3}Ek^{1/2}r_c, \tag{10}$$

where B_{Gr} is a constant whose value should be approximately $Pr^{-1/4} \approx$ 1–3 for molten silicon [11,14].

The surface areas over which these fluxes are acting are determined by straightforward geometrical arguments. The surface area of the crucible wall, A_{cw}, is given by the area of a cylinder with radius r_c and a height determined by the extent of the wetted portion of the wall, which decreases in time as longer lengths of crystal are pulled and the melt volume decreases. Presuming that the crystal radius remains constant,

$$A_{cw} = 2\pi r_c\left(H_0 - \frac{\rho_s}{\rho_m}\frac{r_x^2}{r_c^2}L_x\right), \tag{11}$$

where H_0 is the initial melt depth, ρ_s and ρ_m are the density of solid and liquid silicon, respectively, and L_x is the length of crystal grown. The surface area of the crucible bottom is given by the geometry of the crucible and is taken as a constant, A_{cb}.

Finally, the total oxygen flows from the crucible into the melt for the Ek lumped-parameter model are given by,

$$J_c(A_{cw} + A_{cb}) = \frac{D(A_{cw} + A_{cb})}{\delta_{cw}}(C_c - C_m), \tag{12}$$

and the total oxygen flows from the crucible wall and bottom in the $Ek + Gr$ lumped-parameter model are given by,

$$J_{cw}A_{cw} = \frac{DA_{cw}}{\delta_{cw}}(C_c - C_m), \tag{13}$$

$$J_{cb}A_{cb} = \frac{DA_{cb}}{\delta_{cb}}(C_c - C_m), \tag{14}$$

with all quantities defined as in the section above.

2.2.2. Melt free-surface flux and active area

We assume that we have ideal transport of SiO from the melt surface into the ambient gas. Therefore, all SiO formed at the surface is immediately removed via gas phase transport, and the oxygen concentration at the melt surface takes on the value of zero, $C_s = 0$. This assumption is also used in our 2D-3D model.

To evaluate flows along the free-surface, we utilize the analysis of Okano et al. [43] and presume that these surface flows are driven by gradients in surface tension, so-called Marangoni flow, which are characterized by the Marangoni number,

$$Ma = \frac{-\left(\frac{\partial\sigma}{\partial T}\right)\Delta TL}{\alpha\nu}, \tag{15}$$

where $\frac{\partial\sigma}{\partial T}$ represents the temperature dependence of surface tension, ΔT is the maximum temperature difference across the surface of the melt, and the characteristics length is taken to be distance between the crucible wall and the crystal, $L = r_c - r_x$.

Accordingly, the momentum boundary layer thickness at the free melt surface becomes:

$$\delta_s^{'} = Ma^{-1/3}(r_c - r_x), \tag{16}$$

and the solute boundary thickness is given as,

$$\delta_s = 2.4B_{Ma}Sc^{-1/3}Ma^{-1/3}(r_c - r_x), \tag{17}$$

where B_{Ma} is a constant whose value should be approximately unity.

The area available for oxygen transport across the melt free-surface is affected by the interaction of different flows along the interface. When the crystal is rotated, a centrifugal flow is driven outward along the melt surface. There is a competition between the radially-outward flow driven by crystal rotation and a radially-inward flow that arises from Marangoni forces as well as buoyant flow along the crucible wall that turns inward upon reaching the melt free-surface. If the rotationally-driven flow is strong enough, it pushes outward to create a ring of fluid along the surface, as depicted by the gray region around the crystal in Fig. 1. We furthermore assert that this ring is comprised of fluid that originates from the bulk melt immediately under the melt-crystal interface. We argue that this fluid will be far lower in oxygen concentration than the melt being swept inward along the free surface, which is drawn from the oxygen-rich layer along the dissolving crucible. Thus, the fluid flowing outward from the rotating crystal represents an oxygen-deficient region that spreads outward as a function of crystal rotation rate, reducing the active area of the melt free-surface, which we denote as A_s, that is available for SiO evaporation.

In general, we expect the magnitude of the rotationally-driven outward flow to scale with the rotational Reynolds number,

$$Re_{\omega_x} = \frac{\omega_x r_x^2}{\nu}, \tag{18}$$

which is based on ω_x, the rotation rate of the crystal and r_x, the radius of the crystal.

We presume that the radially-inward flow is dominated by Marangoni effects and that its magnitude scales with $Ma^{2/3}$ [43]. If the radial extent of the oxygen-deficient area scales with these measures of flow magnitude, we argue that the active area available for the transport of oxygen out of the melt is given by,

$$A_s = \pi(r_c^2 - r_x^2)\left(1 - B_A\frac{Re_{\omega_x}}{Ma^{2/3}}\right), \tag{19}$$

where B_A is expected to be of order unity.

This yields a final expression for the molar flow from the melt into the gas phase as,

$$J_a A_s = \frac{DA_s}{\delta_s}(C_m - C_s), \tag{20}$$

where the values of A_s and δ_s are provided by expressions above.

2.2.3. Melt-crystal interface flux

To complete the specification of molar flows into and out of the melt, we consider the incorporation of oxygen into the growing crystal. The flux of oxygen into the crystal is determined by segregation and transport at the melt-crystal interface. We employ a classical depiction of this flux as,

$$J_x = k_{eff} V C_m, \tag{21}$$

where V is the pull rate, C_m is the bulk oxygen concentration in the melt, and k_{eff} is an effective segregation coefficient. The effective segregation coefficient directly relates the concentration of oxygen in the crystal, C_x, to the concentration of oxygen in the bulk melt via,

$$C_x = k_{eff} C_m. \tag{22}$$

We apply the Burton-Prim-Schlichter (BPS) model [44] to provide a value for the effective segregation coefficient as,

$$k_{eff} = \frac{k}{k + (1-k)\exp(-V\delta_x/D)} \tag{23}$$

where k is the equilibrium distribution coefficient, V is is the pull rate, D is the diffusivity of oxygen in silicon, and δ_x is the thickness of the solute boundary layer at the melt-crystal interface. Ostrogorsky [45] provides an estimate of this boundary layer thickness, which is based on Cochran's original analysis of the flow driven by a rotating solid surface [46], as

$$\delta_x = 1.6 D^{1/3} \nu^{1/6} \omega_x^{-1/2}. \tag{24}$$

This yields an expression for the molar flow of oxygen into the crystal, as depicted in Fig. 1, as,

$$J_x A_x = A_x k_{eff} V C_m, \tag{25}$$

where $A_x = \pi r_x^2$ is the area of the melt-crystal interface, which is presumed to be flat in our model.

2.2.4. Melt oxygen concentration

The growth of the crystal is extremely slow with respect to the time scales for oxygen transport. Therefore, we apply a pseudo-steady-state approximation. which asserts that the volume and associated surface areas of the melt region are constant and that the well-mixed melt exhibits a uniform oxygen level, C_m. Under these approximations, $d(V_m C_m)/dt \equiv 0$, and the previous oxygen balance given by Eq. (1) becomes,

$$0 = -J_s A_s - J_x A_x + J_{cw} A_{cw} + J_{cb} A_{cb}. \tag{26}$$

Solving directly for C_m gives,

$$C_m = \frac{C_c F}{F + \frac{A_s}{\delta_s} + \frac{k_{eff} V A_x}{D}}, \tag{27}$$

where

$$F = A_{cw}/\delta_{cw} + A_{cb}/\delta_{cb}. \tag{28}$$

Finally, after solving for the bulk melt concentration, the oxygen level in the growing crystal can be calculated from Eq. (22).

3. Assessment of lumped-parameter models

3.1. Properties and parameters

All properties and parameters employed to compute our lumped-parameter model results are provided in Table 2. Of particular importance are the prefactor coefficients B_i that we employ to calculate thicknesses of the boundary layers. Friedrich et al. [29] used the same boundary-layer correlations as we employ here; however, they simply applied the prefactors from the original power-law expressions. Their model produced surprisingly good correlation with oxygen levels predicted by the 2D-3D model, within approximately a factor of three, while capturing many trends.

Following this previous work, we set the prefactor for the Marangoni boundary layer to the same value as employed by Friedrich et al. [29], namely $B_{Ma} = 1$ in Eq. (17). However, we argue that it is reasonable to choose the prefactors for the Ekman and buoyancy boundary layers, namely B_{Ek} in Eq. (9) and B_{Gr} in Eq. (10), to be different from those in the original fluid mechanical derivations, since their values depend on the specifics of system geometry, such as crucible shape and melt depth.

While one could fit these coefficients to minimize some global measure of error using all data provide from the 2D-3D model, we employ instead a very simple approach. Namely, we choose the values of the three prefactors so that the $Ek + Gr$ lumped-parameter predictions closely match three, selected data points, which are indicated by stars in Fig. 3. These points span different melt depths and crystal rotation rates for the lowest case of crucible rotation. This yields values of $B_{Ek} = 4.65$, $B_{Gr} = 0.072$, and $B_A = 0.067$.

We note that our chosen value for B_{Ek} is reasonably close to the expected value of $B_{Ek} = 3$ given by the geostrophic scaling shown by Eq. (6). However, our fitted value of B_{Gr} is roughly one order of magnitude lower than the expected value of $B_{Gr} = Pr^{-1/4} \approx 1$–$3$ given in Eq. (8). We believe that this may be due to the suppression of buoyant flows by crucible rotation and discuss this matter further in the conclusions section. We believe a similar effect, namely the suppression of Marangoni flows by crucible rotation, may also explain our fitted value of B_A in Eq. (19) being of order 10^{-1} rather than of order unity.

3.2. Model predictions

Figs. 2 and 3 compare the predictions of melt oxygen concentrations, C_m, of the lumped-parameter models to those from the detailed, high-fidelity 2D-3D model simulations [13,14]. Three plots show oxygen concentration in the melt, C_m, as functions of crystal rotation rate, ω_x, for growth runs performed under different crucible rotation rates, ω_c. In each plot, solid blue lines connect melt concentrations predicted by the 2D-3D model, and dashed red or green lines connect the results obtained from the lumped-parameter models. Each plot contains three curves produced by each model that represent results for different melt depths. The upper curves with square points show results for a deep melt, with a short crystal length of 20 mm. The middle curves are marked with circles and represent an intermediate melt depth, with a 1022 mm crystal length. The lowest curves with triangle points represent a shallow melt, with a crystal length of 1684 mm.

3.2.1. 2D-3D predictions

Before comparing the results from the detailed and lumped-parameter models, we present a brief explanation of the physical behaviors responsible for the melt oxygen levels under the different growth conditions. These behaviors are represented by the points connected by the solid blue curves, which show the spatially and temporally averaged melt oxygen concentration from the physically faithful, 2D-3D simulations.

Consider first the left-most plot shown in Fig. 2, which shows cases with a crucible rotation of $\omega_c = -5$ rpm. The effect of melt height on

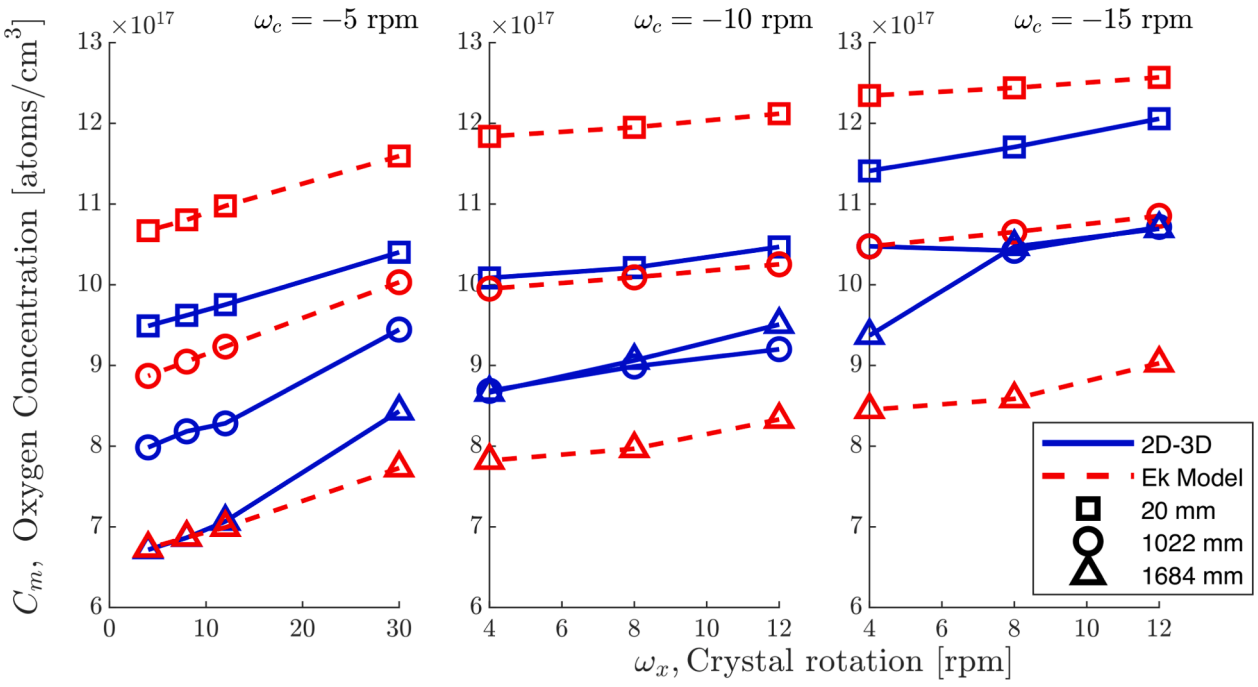

Fig. 2. Comparison of *Ek* lumped-parameter model (red dashed lines) with 2D-3D model predictions (blue solid lines). The melt oxygen concentration is plotted versus crystal rotation for three different crystal body lengths (corresponding to different melt depths). Separate plots are shown for three crucible rotation rates. (For interpretation of the references to color in this figure legend, the reader is referred to the web version of this article.)

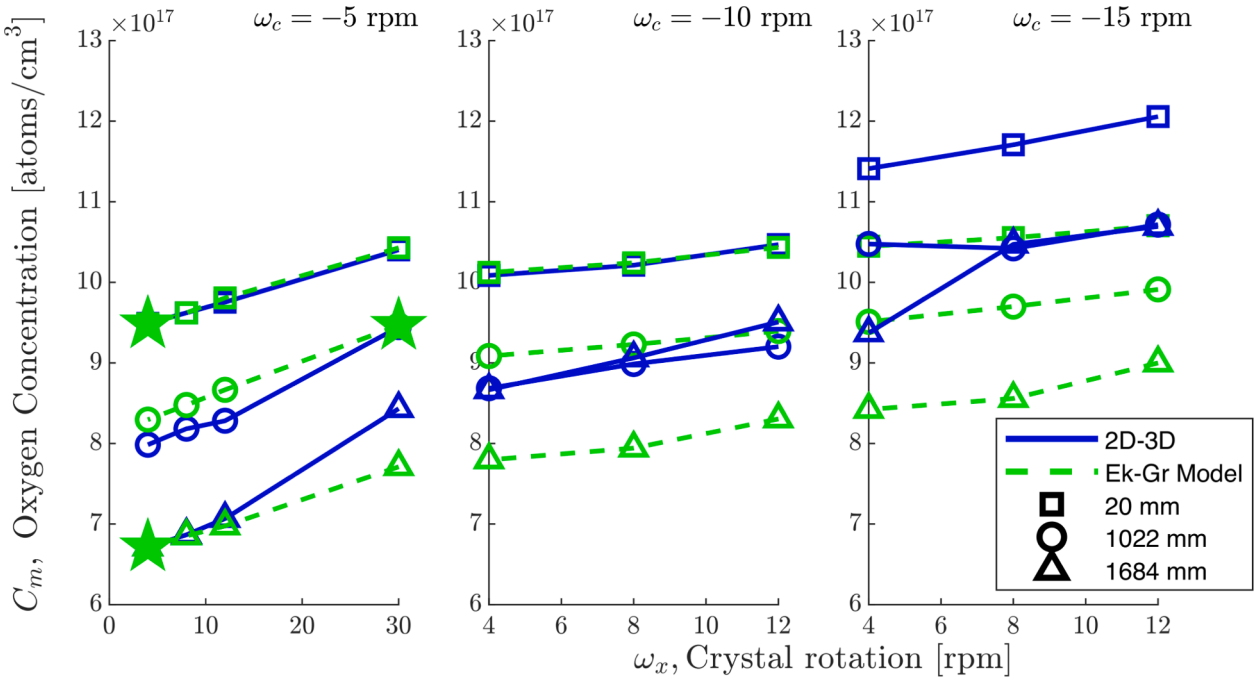

Fig. 3. Comparison of *Ek* + *Gr* lumped-parameter model (red dashed lines) with 2D-3D model predictions (blue solid lines). The melt oxygen concentration is plotted versus crystal rotation for three different crystal body lengths (corresponding to different melt depths). Separate plots are shown for three crucible rotation rates. The stars indicate selected data points used to fit model parameters. (For interpretation of the references to color in this figure legend, the reader is referred to the web version of this article.)

oxygen concentration is shown by the three different solid blue curves in this plot. Melt oxygen concentration decreases as the melt level drops with longer crystals, progressing from a 20 mm crystal length (square data points) to 1022 mm (circles) to 1684 mm (triangles). This decrease in melt oxygen is caused by the smaller wetted crucible surface area as the melt level drops. The smaller area of dissolving crucible reduces the flux of oxygen into the melt, thereby reducing C_m.

The drop in melt oxygen concentration is observed only from the highest to intermediate melt levels for cases of higher crucible rotation, $\omega_c = -10$ rpm and $\omega_c = -15$ rpm. For these higher crucible rotation rates, the curves for the shallower melt depth are very nearly the same. We postulate that the suppression of buoyant flows is stronger at higher

crucible rotation, so that oxygen dissolution into the melt is lessened from the crucible wall. Hence, the overall flux of oxygen into the melt is dominated by dissolution from the bottom of the crucible, making the melt height unimportant below a certain level.

The transport of oxygen increases through thinner Ekman layers that arise at faster crucible rotation rates, giving rise to generally higher levels of melt oxygen concentration for faster crucible rotation.

Finally, the 2D-3D simulations show that the oxygen concentration in the melt always increases with crystal rotation rate, ω_x. As discussed in the derivation of the lumped-parameter model in Section 2.2.2, we assert that radially-outward flows from crystal rotation counter the radially-inward flows driven by Marangoni effects, thus limiting the amount of surface area for the evaporation of SiO from the melt. As the crystal is rotated faster, the active surface area available for oxygen transport decreases. With reduced surface area for oxygen transport along the melt free-surface, the overall oxygen flow is decreased and the melt concentration is increased.

3.2.2. Lumped-parameter model predictions

The results of the simpler *Ek* lumped-parameter model are shown by the dashed red curves in Fig. 2. This model matches the 2D-3D simulations almost exactly for the cases corresponding to the longest crystal length and shallowest melt (triangles). This agreement is no doubt aided by choosing three data points from the 2D-3D model results from the slow crucible rotation case of $\omega_c = -5$ rpm to fit coefficients in the lumped-parameter model, as described previously. We observe that the general lumped-parameter model predictions on the effects of crystal rotation on melt oxygen concentration levels are quite good for all cases, as shown by the good approximations to the slopes of the curves.

The effect of melt height (crystal length) on melt oxygen concentration is qualitatively represented by the *Ek* lumped-parameter model; however, its effect is exaggerated in this simple model. Observe that the dashed red lines are too widely separated from the corresponding solid blue lines from the 2D-3D model, indicating that the changing melt level too strongly affects the predictions. Consistent with this effect, even though the general trend of higher melt oxygen levels with higher crucible rotation rates is predicted by the *Ek* lumped-parameter model, the quantitative predictions for different melt levels do not agree with the 2D-3D simulations.

The deficiencies of the *Ek* lumped-parameter model in accounting for the effects of melt level are better addressed by the *Ek* + *Gr* lumped-parameter model, whose predictions are shown in Fig. 3. By separately accounting for crucible wall fluxes that are independent from crucible bottom fluxes, this model is able to more accurately represent oxygen levels in the melt at the higher crucible rotation rates of $\omega_c = -10$ and $\omega_c = -15$ rpm. However, the *Ek* + *Gr* lumped-parameter model still struggles to capture the more complicated behaviors associated with higher crucible rotation, such as the near overlay of the oxygen levels for the shallow melt cases. We further discuss this shortcoming in the following section.

4. Discussion and conclusions

We have derived and assessed physically-based, lumped-parameter models that calculate oxygen levels in Czochralski silicon crystal growth melts as functions of growth parameters. These lumped-parameter models, which describe oxygen transport using only simple algebraic equations, allow nearly instantaneous calculation of the oxygen concentration on any computer. We assert that fast computations provided by such lumped-parameter models may make them suitable for real-time optimization and control, tasks that are not served well by the very long computation times required by more sophisticated models

Our assessment shows that the *Ek* + *Gr* lumped-parameter model performs reasonably well in predicting oxygen levels, faithfully representing trends with process parameters and providing melt oxygen concentration predictions that are typically within 20% of those obtained by the 2D-3D model. An important advance of the lumped-parameter model developed here over the previous model of Friedrich et al. [29] is its ability to well represent the effects of crystal rotation.

We believe that our lumped-parameter model could be further improved via a more complete consideration of the interactions between buoyant flows and crucible rotation. While the independent consideration of these effects in the *Ek* + *Gr* lumped-parameter model improved predictions over the simpler *Ek* lumped-parameter model, our calculation of the boundary layer thickness along the vertical wall, Eq. (8), considered only the magnitude of the Grashof number. We believe that crucible rotation should also be included in this estimate for wall transport, since the centrifugal forces caused by crucible rotation will suppress buoyant flow. Such a modification may better represent the system behavior at higher crucibles rotation rates.

In any model, care must be exercised with respect to any fitting of coefficients. John von Neumann is purported to have said about such models, "with four parameters I can fit an elephant and with five I can make him wriggle his trunk" [47]. Here, we employed very simple procedures using data that reflected dominant effects caused by physical phenomena associated with the fitted coefficients. In addition, we have strived to justify the values of our fitted values by comparing them to values expected from the scaling laws employed by the model. More sophisticated error-minimization techniques would certainly produce coefficients that result in more accurate model predictions. It may also be reasonable to fit the Marangoni coefficient B_{Ma}, which was not fit from our data, for more accurate lumped-parameter model predictions.

Extensions of the model to take into account other effects, such as magnetic fields applied across the melt or different gas flow patterns through the puller, are likely with a physical understanding of how these additional processes affect flow structures and associated oxygen transport in the melt. Also of possible interest is the use of transient, rather than quasi-steady, lumped-parameter models to study time-dependent changes in oxygen levels due to changes in growth parameters or control actions. Such approaches proved very valuable toward gaining a better understanding of transient phenomena in stirred-tank chemical reactors [23–26].

We conclude with a quote from Alex Chernov from the Sixth International Conference on Crystal Growth, ICCG-6, Moscow, 1980 [48]: "Young people know how to play the piano on a computer keyboard, but sometimes it is necessary to go back to simple calculations and estimations in order to find the necessary answers. So it always comes down to a combination of computer modeling and basic initial approaches, as well as a simple back-of-the-envelope sketch." Well-constructed, physically-based lumped-parameter models are exactly these simple back-of-the-envelope sketches that help us understand what is going on in complex crystal growth systems.

CRediT authorship contribution statement

Kerry Wang: Methodology, Investigation, Software, Visualization, Writing – original draft. **Holger Koch:** Methodology, Investigation, Resources, Writing – review & editing. **Matthias Trempa:** Methodology, Investigation, Resources, Writing – review & editing. **Christian Kranert:** Methodology, Investigation, Resources, Writing – review & editing. **Jochen Friedrich:** Conceptualization, Supervision, Methodology, Investigation, Funding acquisition, Writing – review & editing. **Jeffrey J. Derby:** Conceptualization, Project administration, Supervision, Funding acquisition, Writing – review & editing.

Declaration of Competing Interest

The authors declare that they have no known competing financial interests or personal relationships that could have appeared to influence the work reported in this paper.

Acknowledgements

The authors would like to acknowledge partial support of this work from the University of Minnesota and the *CZ3003* project, funded partly by the German Federal Ministry for Economic Affairs and Energy (BMWi) under contract number 0324357A. The authors would like to thank Dr. Thomas Jung for significant, original contributions. We also wish to thank an anonymous reviewer, whose comments substantially improved the paper.

References

[1] J.J. Derby, R.A. Brown, Thermal-capillary analysis of Czochralski and liquid encapsulated Czochralski crystal growth, I. Simulation, J. Cryst. Growth 74 (1986) 605–624.
[2] J.J. Derby, R.A. Brown, Thermal-capillary analysis of Czochralski and liquid encapsulated Czochralski crystal growth, II. Processing strategies, J. Cryst. Growth 75 (1986) 227–240.
[3] J.J. Derby, L.J. Atherton, P.D. Thomas, R.A. Brown, Finite element methods for analysis of the dynamics and control of Czochralski crystal growth, J. Sci. Comput. 2 (4) (1987) 297–343.
[4] J.J. Derby, R.A. Brown, On the dynamics of Czochralski crystal growth, J. Cryst. Growth 83 (1987) 137–151.
[5] L.J. Atherton, J.J. Derby, R.A. Brown, Radiative heat exchange in Czochralski crystal growth, J. Cryst. Growth 84 (1987) 57.
[6] J.J. Derby, R.A. Brown, On the quasi-steady-state assumption in modeling Czochralski crystal growth, J. Cryst. Growth 87 (1988) 251–260.
[7] P.A. Sackinger, R.A. Brown, J.J. Derby, A finite-element method for analysis of fluid flow, heat transfer and free interfaces in Czochralski crystal growth, Int. J. Numer. Meth. Fluids 9 (1989) 453–492.
[8] F. Dupret, P. Nicodème, Y. Ryckmans, P. Wouters, M.J. Crochet, Global modelling of heat transfer in crystal growth furnaces, Int. J. Heat Mass Transf. 33 (1990) 1849–1871.
[9] Koichi Kakimoto, Pierre Nicodème, Michael Lecomte, François Dupret, Marcel J. Crochet, Numerical simulation of molten silicon flow; comparison with experiment, J. Cryst. Growth 114 (4) (1991) 715–725.
[10] I.Yu. Evstratov, V.V. Kalaev, A.I. Zhmakin, Yu.N. Makarov, A.G. Abramov, N. G. Ivanov, E.M. Smirnov, E. Dornberger, J. Virbulis, E. Tomzig, W. von Ammon, Modeling analysis of unsteady three-dimensional turbulent melt flow during Czochralski growth of Si crystals, J. Cryst. Growth 230 (1) (August 2001) 22–29.
[11] D.P. Lukanin, V.V. Kalaev, Yu.N. Makarov, T. Wetzel, J. Virbulis, W. von Ammon, Advances in the simulation of heat transfer and prediction of the melt-crystal interface shape in silicon CZ growth, J. Cryst. Growth 266 (1) (May 2004) 20–27.
[12] A.D. Smirnov, V.V. Kalaev, Development of oxygen transport model in Czochralski growth of silicon crystals, J. Cryst. Growth 310 (12) (June 2008) 2970–2976.
[13] A. Krauze, N. Jēkabsons, A. Muižnieks, A. Sabanskis, U. Lācis, Applicability of LES turbulence modeling for CZ silicon crystal growth systems with traveling magnetic field, J. Cryst. Growth 312 (21) (October 2010) 3225–3234.
[14] T. Jung, J. Seebeck, J. Friedrich, Combined global 2D–local 3D modeling of the industrial Czochralski silicon crystal growth process, J. Cryst. Growth 368 (April 2013) 72–80.
[15] Jochen Friedrich, Thomas Jung, Matthias Trempa, Christian Reimann, Alexey Denisov, Andreas Muehe, Considerations on the limitations of the growth rate during pulling of silicon crystals by the Czochralski technique for PV applications, J. Cryst. Growth 524 (2019) 125168.
[16] R. Yokoyama, T. Nakamura, W. Sugimura, T. Ono, T. Fujiwara, K. Kakimoto, Time-dependent behavior of melt flow in the industrial scale silicon Czochralski growth with a transverse magnetic field, J. Cryst. Growth 519 (2019) 77–83.
[17] Jing Zhang, Jun-Chao Ren, Ding Liu, Effect of crucible rotation and crystal rotation on the oxygen distribution at the solid-liquid interface during the growth of Czochralski monocrystalline silicon under superconducting horizontal magnetic field, Res. Phys. 13 (2019) 102127.
[18] Vladimir Kalaev, Computer modeling of HMCz Si growth, J. Cryst. Growth 532 (2020) 125413.
[19] Michael A. Gevelber, George Stephanopoulos, Dynamics and control of the Czochralski process: I. Modelling and dynamic characterization, J. Cryst. Growth 84 (4) (1987) 647–668.
[20] Michael A. Gevelber, George Stephanopoulos, Michael J. Wargo, Dynamics and control of the Czochralski process II. Objectives and control structure design, J. Cryst. Growth 91 (1) (1988) 199–217.
[21] Paul Sonda, Andrew Yeckel, Prodromos Daoutidis, Jeffrey J. Derby, Development of model-based control for Bridgman crystal growth, J. Cryst. Growth 266 (2004) 182–189.
[22] J. Winkler, M. Neubert, Automation of crystal growth from melt, in: T. Nishinaga, P. Rudolph (Eds.), Handbook of Crystal Growth, second ed., vol. II, Part A, Elsevier, 2015, pp. 1143–1184 (Chapter 28).
[23] Rutherford Aris, Neal R. Amundson, An analysis of chemical reactor stability and control—I: The possibility of local control, with perfect or imperfect control mechanisms, Chem. Eng. Sci. 7 (3) (1958) 121–131.
[24] A. Uppal, W.H. Ray, A.B. Poore, On the dynamic behavior of continuous stirred tank reactors, Chem. Eng. Sci. 29 (1974) 967.
[25] I.G. Kevrekidis, R. Aris, L.D. Schmidt, The stirred tank forced, Chem. Eng. Sci. 41 (6) (1986) 1549–1560.
[26] R. Aris, Mathematical Modeling: A Chemical Engineer's Perspective, Academic Press, 1999.
[27] Torbjorn Carlberg, Thomas B. King, August F. Witt, Dynamic Oxygen Equilibrium in Silicon Melts during Crystal Growth by the Czochralski Technique, J. Electrochem. Soc. 129 (1) (January 1982) 189–193.
[28] Keigo Hoshikawa, Xinming Huang, Oxygen transportation during Czochralski silicon crystal growth, Mater. Sci. Eng. B 72 (2) (March 2000) 73–79.
[29] J. Friedrich, M. Trempa, H. Koch, F. Mosel, Comparison of the oxygen concentration in Czochralski silicon crystal obtained by a simple lumped-parameter model and sophisticated 2D-3D simulations, in: EU PVSection 2021 Conference Proceedings. 38th European Photovoltaic Solar Energy Conference and Exhibition, 2021.
[30] J. Fainberg, D. Vizman, J. Friedrich, G. Mueller, A new hybrid method for the global modeling of convection in CZ crystal growth configurations, J. Cryst. Growth 303 (1) (2007) 124–134.
[31] M. Kurz, A. Pusztai, G. Müller, Development of a new powerful computer code CrysVUN++ especially designed for fast simulation of bulk crystal growth processes, J. Cryst. Growth 198–199 (1999) 101–106.
[32] OpenCFD, OpenFOAM - Official home of The Open Source Computational Fluid Dynamics (CFD) Toolbox. http://www.openfoam.com.
[33] Jochen Friedrich, Wilfried von Ammon, Georg Müller, Czochralski growth of silicon crystals, in: T. Nishinaga, P. Rudolph (Eds.), Handbook of Crystal Growth, second ed., vol. II, Part A, Elsevier, 2015, pp. 45–104 (Chapter 7).
[34] Hermann Schlichting, Klaus Gersten, Boundary Layer Theory, 8th edition., Springer-Verlag, 2004.
[35] W.M. Deen, Analysis of Transport Phenomena, Topics in Chemical Engineering, second ed., Oxford University Press, 2012.
[36] Bhushan Vartak, Andrew Yeckel, Jeffrey J. Derby, On the validity of boundary layer analysis for flow and mass transfer caused by rotation during the solution growth of large, single crystals, J. Cryst. Growth 283 (3) (2005) 479–489.
[37] Shinji Togawa, Xinming Huang, Koji Izunome, Kazutaka Terashima, Shigeyuki Kimura, Oxygen transport analysis in Czochralski silicon melt by considering the oxygen evaporation from the melt surface, J. Cryst. Growth 148 (1) (February 1995) 70–78.
[38] Koichi Kakimoto, Kyung-Woo Yi, Minoru Eguchi, Oxygen transfer during single silicon crystal growth in Czochralski system with vertical magnetic fields, J. Cryst. Growth 163 (3) (1996) 238–242.
[39] Mingwei Li, Yourong Li, Nobuyuki Imaishi, Takao Tsukada, Global simulation of a silicon Czochralski furnace, J. Cryst. Growth 234 (1) (2002) 32–46.
[40] Jyh-Chen Chen, Ying-Yang Teng, Wan-Ting Wun, Chung-Wei Lu, Hsueh-I. Chen, Chi-Yung Chen, Wen-Chieh Lan, Numerical simulation of oxygen transport during the CZ silicon crystal growth process, J. Cryst. Growth 318(1) (2011) 318–323.
[41] E.M. King, S. Stellmach, B. Buffett, Scaling behaviour in Rayleigh-Bénard convection with and without rotation, J. Fluid Mech. 717 (February 2013) 449–471.
[42] A.E. Gill, The boundary-layer regime for convection in a rectangular cavity, J. Fluid Mech. 26 (3) (1966) 515–536.
[43] Yasunori Okano, Masato Tachibana, Ako Hatano, Akira Hirata, Control of Crystal-Melt Interface Shape during Czochralski Growth of Oxide Single Crystals, J. Chem. Eng. Jpn. 22 (4) (1989) 389–394.
[44] J.A. Burton, R.C. Prim, W.P. Slichter, The Distribution of Solute in Crystals Grown from the Melt. Part I. Theoretical, J. Chem. Phys. 21 (11) (November 1953) 1987–1991.
[45] Aleksandar G. Ostrogorsky, Georg Müller, A model of effective segregation coefficient, accounting for convection in the solute layer at the growth interface, J. Cryst. Growth 121 (4) (1992) 587–598.
[46] W.G. Cochran, The flow due to a rotating disc, Proc. Camb. Phil. Soc. 30 (1934) 365–375.
[47] Jeffrey H. Williams, Data fitting and elephants, in: Quantifying Measurement, 2053–2571, Morgan & Claypool Publishers, 2016, pages 10–1 to 10–16.
[48] Peter Rudolph, Meine Heimat ist die Wissenschaft – zum 90. Geburtstag von Prof. Dr. A.A. Chernov [Science is my home – on the 90th birthday of Prof. Dr. A.A. Chernov]. DGKK-Mitteilungsblatt [German Association for Crystal Growth Newsletter], 111, 2021.